Reconstructing Spatio-Temporal Activities of Neural Sources Using an MEG Vector Beamformer Technique

Kensuke Sekihara*, *Member, IEEE*, Srikantan S. Nagarajan, David Poeppel, Alec Marantz, and Yasushi Miyashita

***Abstract*—We have developed a method suitable for reconstructing spatio-temporal activities of neural sources by using magnetoencephalogram (MEG) data. The method extends the adaptive beamformer technique originally proposed by Borgiotti and Kaplan to incorporate the vector beamformer formulation in which a set of three weight vectors are used to detect the source activity in three orthogonal directions. The weight vectors of the vector-extended version of the Borgiotti–Kaplan beamformer are then projected onto the signal subspace of the measurement covariance matrix to obtain the final form of the proposed beamformer's weight vectors. Our numerical experiments show that both spatial resolution and output signal-to-noise ratio of the proposed beamformer are significantly higher than those of the minimum-variance-based vector beamformer used in previous investigations. We also applied the proposed beamformer to two sets of auditory-evoked MEG data, and the results clearly demonstrated the method's capability of reconstructing spatio-temporal activities of neural sources.**

***Index Terms*—Beamformer, biomagnetism, functional neuroimaging, magnetoencephalography, MEG inverse problems, neuromagnetic signal processing.**

I. Introduction

AMONG the various kinds of functional neuroimaging methodologies, the major advantage of magnetoencephalography (MEG) is its ability to provide fine time resolution of the millisecond order [1]. Neuromagnetic imaging can thus be used to visualize neural activities with such a fine time resolution, and to provide functional information about brain dynamics [2]. Toward this goal, a number of algorithms for reconstructing spatio-temporal source activities have been developed. Well-known approaches for this reconstruction employ the model of the equivalent current dipole (ECD) [3], which assumes a highly localized source. Although this ECD model has successfully been applied to neuromagnetic data, we cannot rely on ECD modeling when the source is distributed or when no information on the spatial extent of the source is available.

Another approach for spatio-temporal reconstruction is based on the linear estimation method [4]; it assumes voxels in the reconstruction region and attempts to estimate the moment of a source assigned to each voxel by using least-squares fitting. Although this approach does not impose any models on the neuromagnetic source, a naive form of such an approach has a serious problem in that the estimation becomes severely ill posed. This is because the number of voxels generally reaches, at least, a few thousand, so several thousand parameters need to be estimated from the measured data obtained at only one to two hundred points on the scalp surface. To reduce the influence from this ill-posed condition, an efficient method of constraining the least-squares solution should be developed. This has been an area of active research, and many kinds of investigations in this direction have been reported [5]–[7].

In this paper, we explore the possibility of applying a class of techniques called the adaptive beamformer to this reconstruction problem. The adaptive beamformer provides a versatile form of spatial filtering suitable for processing data from an array of sensors. Adaptive-beamformer-type techniques were originally developed in the fields of array signal processing, including radar, sonar, and seismic exploration [8], and they have been already applied to the MEG/EEG source-reconstruction problem [9]–[12]. In these investigations, the minimum-variance beamformer, which is one of most popular adaptive beamformer techniques, was modified to incorporate the detection of three-dimensional (3-D) vector sources. Particularly, in [9], [10], [12], a vector beamformer technique has been developed on the basis of the minimum-variance beamformer; the vector beamformer uses a set of three weight vectors for detecting the source activity in three orthogonal directions such as x, y, and z, thereby reconstructing not only the source magnitude but also the source orientation.

This paper develops a vector beamformer technique on the basis of the Borgiotti–Kaplan beamformer [13]. The developed beamformer performs significantly better than the minimum-variance beamformer used in the previous investigations, with respect to the spatial resolution and the output signal-to-noise ratio (SNR). In Section II, after a brief introduction to the minimum-variance-based beamformer technique, we formulate our proposed vector beamformer. In Section III, a series of numerical experiments verify the effectiveness of the proposed beam-

Manuscript received March 17, 2000; revised April 6, 2001. The work of S. S. Nagarajan was supported by a grant from the Whitaker Foundation. This work was carried out as part of the MIT-JST International Cooperative Research Project "Mind Articulation." *Asterisk indicates corresponding author.*

*K. Sekihara is with the Department of Electronic Systems and Engineering, Tokyo Metropolitan Institute of Technology, Asahigaoka 6-6, Hino, Tokyo 191-0065, Japan (e-mail: ksekiha@cc.tmit.ac.jp).

S. S. Nagarajan is with the Department of Bioengineering, University of Utah, Salt Lake City, UT 84112-9202 USA.

D. Poeppel is with the Department of Linguistics and Biology, University of Maryland, College Park, MD 20742 USA.

A. Marantz is with the Department of Linguistics and Philosophy, Massachusetts Institute of Technology, Cambridge, MA 02139 USA.

Y. Miyashita is with the Department of Physiology, The University of Tokyo, School of Medicine, Hongo, Tokyo 113-0033, Japan.

Publisher Item Identifier S 0018-9294(01)05134-5.

former. In Section IV, we apply the proposed beamformer to two sets of auditory MEG data. The results of these applications demonstrate its capability of reconstructing spatio-temporal activities of neural sources. Throughout this paper, plain italics indicate scalars, lower-case boldface italics indicate vectors, and upper-case boldface italics indicate matrices.

II. Method

A. Definitions and Problem Formulation

Let us define the magnetic field measured by the mth detector coil at time t as $b_m(t)$, and a column vector $\boldsymbol{b}(t) = [b_1(t), b_2(t), \ldots, b_M(t)]^T$ as a set of measured data where M is the total number of detector coils and the superscript T indicates the matrix transpose. A spatial location (x, y, z) is represented by a 3-D vector $\boldsymbol{r}$: $\boldsymbol{r} = (x, y, z)$. A total of Q current sources are assumed to generate the neuromagnetic field, and the locations of these sources are denoted as $\boldsymbol{r}_1, \boldsymbol{r}_2, \ldots, \boldsymbol{r}_Q$. The moment magnitude of the qth source at time t is defined as $s_q(t)$, and the source magnitude vector is defined as $\boldsymbol{s}(t) = [s_1(t), s_2(t), \ldots, s_Q(t)]^T$.

To express the orientation of the qth source, we define the angles between its moment vector and the x, y, and z axes as $\beta_q^x(t)$, $\beta_q^y(t)$, and $\beta_q^z(t)$, respectively. The orientation of the qth source is defined as a vector $\boldsymbol{\eta}_q(t) = [\eta_q^x(t), \eta_q^y(t), \eta_q^z(t)]^T$, where $\eta_q^\mu(t) = \cos[\beta_q^\mu(t)]$ and μ is equal to x, y, or z throughout this paper. We define a $3Q \times Q$ matrix that expresses the orientations of all Q sources as $\boldsymbol{\Psi}$ such that

$$\boldsymbol{\Psi} = \begin{bmatrix} \boldsymbol{\eta}_1 & 0 & \cdots & 0 \\ 0 & \boldsymbol{\eta}_2 & \cdot & \vdots \\ \vdots & \cdot & \ddots & 0 \\ 0 & \cdots & 0 & \boldsymbol{\eta}_Q \end{bmatrix}.$$

We assume in this paper that the orientation of each source is time independent.

The lead field vector for the μ component of a source at $\boldsymbol{r}$ is defined as $\boldsymbol{l}_\mu(\boldsymbol{r}) = [l_1^\mu(\boldsymbol{r}), l_2^\mu(\boldsymbol{r}), \ldots, l_M^\mu(\boldsymbol{r})]^T$. Here, $l_m^\mu(\boldsymbol{r})$ expresses the mth sensor output induced by the unit-magnitude source that is located at $\boldsymbol{r}$ and directed in the μ direction. We define the lead field matrix as $\boldsymbol{L}(\boldsymbol{r}) = [\boldsymbol{l}_x(\boldsymbol{r}), \boldsymbol{l}_y(\boldsymbol{r}), \boldsymbol{l}_z(\boldsymbol{r})]$, which represents the sensitivity of the sensor array at $\boldsymbol{r}$. The lead field vector representing the sensitivity of a sensor array in the $\boldsymbol{\eta}$ direction at $\boldsymbol{r}$ is denoted as $\boldsymbol{l}(\boldsymbol{r}, \boldsymbol{\eta})$, which is calculated from $\boldsymbol{l}(\boldsymbol{r}, \boldsymbol{\eta}) = \boldsymbol{L}(\boldsymbol{r})\boldsymbol{\eta}^T$. The composite lead field matrix for the entire set of Q sources is defined as

$$\boldsymbol{L}_c = [\boldsymbol{L}(\boldsymbol{r}_1), \boldsymbol{L}(\boldsymbol{r}_2), \ldots, \boldsymbol{L}(\boldsymbol{r}_Q)]. \tag{1}$$

The relationship between $\boldsymbol{b}(t)$ and $\boldsymbol{s}(t)$ is then expressed as

$$\boldsymbol{b}(t) = (\boldsymbol{L}_c\boldsymbol{\Psi})\boldsymbol{s}(t) + \boldsymbol{n}(t) \tag{2}$$

where $\boldsymbol{n}(t)$ is the additive noise. We define, for later use, the covariance matrix of the measured magnetic field as $\boldsymbol{R}_b$ such that $\boldsymbol{R}_b = \langle(\boldsymbol{b}(t) - \langle\boldsymbol{b}(t)\rangle)(\boldsymbol{b}(t) - \langle\boldsymbol{b}(t)\rangle)^T\rangle$ where $\langle\cdot\rangle$ indicates the ensemble average.

To estimate the source moment from the measured magnetic field, we focus on the class of techniques referred to as a beamformer [8]. The beamformer technique estimates the moment magnitude of a source located at $\boldsymbol{r}$ and directed in the $\boldsymbol{\eta}$ direction using the following linear spatial filter operation:

$$\hat{s}(\boldsymbol{r}, \boldsymbol{\eta}, t) = \boldsymbol{w}^T(\boldsymbol{r}, \boldsymbol{\eta})\boldsymbol{b}(t) \tag{3}$$

where $\hat{s}(\boldsymbol{r}, \boldsymbol{\eta}, t)$ is the estimated moment magnitude. In (3), the column vector $\boldsymbol{w}(\boldsymbol{r}, \boldsymbol{\eta})$ represents a set of weights that characterizes the property of the beamformer. It should be pointed out that according to (3), the power of the output noise due to the additive white noise $\boldsymbol{n}(t)$ is proportional to $\langle|\boldsymbol{w}^T\boldsymbol{n}(t)|^2\rangle = \sigma^2\boldsymbol{w}^T\boldsymbol{w}$ where $\boldsymbol{n}(t)$ is assumed to be the white Gaussian noise and σ^2 is its variance. That is, the power of the output noise is proportional to $\boldsymbol{w}^T\boldsymbol{w}$, which is called the white noise gain for this reason.

B. Existing Beamformer Techniques for Reconstructing Neural Source Activities

1) Minimum-Variance Distortionless Beamformer: One well-known beamformer technique is the minimum-variance distortionless beamformer [14], in which the weight vector $\boldsymbol{w}$ is obtained by minimizing $\boldsymbol{w}^T\boldsymbol{R}_b\boldsymbol{w}$ with the constraint of $\boldsymbol{w}^T\boldsymbol{l}(\boldsymbol{r}, \boldsymbol{\eta}) = 1$. (Although the weight vector depends on the pointing location $\boldsymbol{r}$, we omit the explicit notation of $\boldsymbol{r}$ unless this omission causes ambiguity.) This weight vector is

$$\boldsymbol{w}(\boldsymbol{r}, \boldsymbol{\eta}) = \frac{\boldsymbol{R}_b^{-1}\boldsymbol{l}(\boldsymbol{r}, \boldsymbol{\eta})}{\boldsymbol{l}^T(\boldsymbol{r}, \boldsymbol{\eta})\boldsymbol{R}_b^{-1}\boldsymbol{l}(\boldsymbol{r}, \boldsymbol{\eta})}. \tag{4}$$

This minimum-variance beamformer is widely used in various signal-processing fields. One problem arises when we apply it to reconstructing neural sources. That is, to calculate the beamformer weight by using (4), we must first determine the source orientation $\boldsymbol{\eta}$ at each $\boldsymbol{r}$. This determination is not straightforward, although a method have been proposed for this purpose [15].

2) Vector-Extension of Minimum-Variance Beamformer: Instead of estimating the source orientation and magnitude separately, the minimum-variance beamformer can be modified to estimate not only the source magnitude but also the source orientation. Such a beamformer simultaneously estimates the source moment in three orthogonal directions such as x, y, and z. Let us denote the unit vectors in the x, y, and z directions, as $\boldsymbol{f}_x$, $\boldsymbol{f}_y$, and $\boldsymbol{f}_z$, respectively, i.e., $\boldsymbol{f}_x = [1, 0, 0]^T$, $\boldsymbol{f}_y = [0, 1, 0]^T$, and $\boldsymbol{f}_z = [0, 0, 1]^T$. Let us also denote the weight vectors that estimate $\hat{s}_x(t)$, $\hat{s}_y(t)$, and $\hat{s}_z(t)$ as $\boldsymbol{w}_x$, $\boldsymbol{w}_y$, and $\boldsymbol{w}_z$. Then, these weight vectors can be derived by the following minimizations with multiple constraints:

$$\min_{\boldsymbol{w}_x} \boldsymbol{w}_x^T\boldsymbol{R}_b\boldsymbol{w}_x$$

subject to

$$\boldsymbol{w}_x^T\boldsymbol{l}_x(\boldsymbol{r}) = 1, \quad \boldsymbol{w}_x^T\boldsymbol{l}_y(\boldsymbol{r}) = 0, \quad \text{and} \quad \boldsymbol{w}_x^T\boldsymbol{l}_z(\boldsymbol{r}) = 0,$$

$$\min_{\boldsymbol{w}_y} \boldsymbol{w}_y^T\boldsymbol{R}_b\boldsymbol{w}_y$$

subject to

$$\boldsymbol{w}_y^T\boldsymbol{l}_x(\boldsymbol{r}) = 0, \quad \boldsymbol{w}_y^T\boldsymbol{l}_y(\boldsymbol{r}) = 1, \quad \text{and} \quad \boldsymbol{w}_y^T\boldsymbol{l}_z(\boldsymbol{r}) = 0,$$

$$\min_{\boldsymbol{w}_z} \boldsymbol{w}_z^T\boldsymbol{R}_b\boldsymbol{w}_z$$

subject to

$$\boldsymbol{w}_z^T \boldsymbol{l}_x(\boldsymbol{r}) = 0, \quad \boldsymbol{w}_z^T \boldsymbol{l}_y(\boldsymbol{r}) = 0, \quad \text{and} \quad \boldsymbol{w}_z^T \boldsymbol{l}_z(\boldsymbol{r}) = 1. \quad (5)$$

The minimum-variance beamformer with multiple linear constraints, referred to as the linearly constrained minimum-variance beamformer, is known to have the following solution [9], [10]:

$$[\boldsymbol{w}_x, \boldsymbol{w}_y, \boldsymbol{w}_z] = \boldsymbol{R}_b^{-1} \boldsymbol{L}(\boldsymbol{r}) \left[\boldsymbol{L}^T(\boldsymbol{r}) \boldsymbol{R}_b^{-1} \boldsymbol{L}(\boldsymbol{r})\right]^{-1} \boldsymbol{\Phi} \quad (6)$$

where $\boldsymbol{\Phi}$ is defined as $\boldsymbol{\Phi} = [\boldsymbol{f}_x, \boldsymbol{f}_y, \boldsymbol{f}_z]$.

Equation (5) indicates that, when estimating one of the three orthogonal components of the source moment, we need to suppress the other two components. This is because when estimating one of the three components, the other two components behave like perfectly correlated virtual sources. Therefore, without this suppression, considerable amount of signal cancellation should arise. By applying these null constraints, however, we can avoid this signal cancellation, and the beamformer can detect the source moment projected in three orthogonal directions. Such a beamformer is referred to as a vector beamformer.

There are two problems when applying (6) to actual MEG/EEG source reconstruction problems. First, the beamformer output has erroneously large values near the center of the sphere used for the forward calculation. This is because $||\boldsymbol{L}(\boldsymbol{r})||$ becomes very small when $\boldsymbol{r}$ approaches the center of the sphere. To avoid these $||\boldsymbol{L}(\boldsymbol{r})||$-dependent artifacts, the use of the normalized lead field matrix $\boldsymbol{L}(\boldsymbol{r})/||\boldsymbol{L}(\boldsymbol{r})||$ has been suggested [10], [12].

Second, the performance of the beamformer in (6) is very sensitive to errors in calculating the lead field matrix, when applied to the spatio-temporal reconstruction of the source activities [15]. This problem is known to be partly solved by replacing $\boldsymbol{R}_b^{-1}$ in (6) with its regularized inverse $(\boldsymbol{R}_b + \gamma \boldsymbol{I})^{-1}$ [11], [12], [16], [17] where the parameter γ is the regularization parameter. Such replacement, however, is known to degrade the spatial resolution, providing a tradeoff between the SNR and the spatial resolution [11]. In the following section, we propose a beamformer that is free from this tradeoff and can attain an inherently higher spatial resolution.

C. Formulation of the Proposed Method

The proposed beamformer is formulated on the basis of the beamformer developed by Borgiotti and Kaplan [13]; its weight vector is derived by minimizing $\boldsymbol{w}^T \boldsymbol{R}_b \boldsymbol{w}$ with the constraint of $\boldsymbol{w}^T \boldsymbol{w} = 1$. Because the Borgiotti–Kaplan beamformer has the unit white noise gain, the output power of the Borgiotti–Kaplan beamformer is equal to the power of the signal normalized by the power of the noise [13]. The weight vectors of the proposed beamformer are derived by a two-step procedure. The first step extends the Borgiotti–Kaplan beamformer to the vector-type beamformer. The second step further extends this vector-extended version of the Borgiotti–Kaplan beamformer to an eigenspace-projected beamformer.

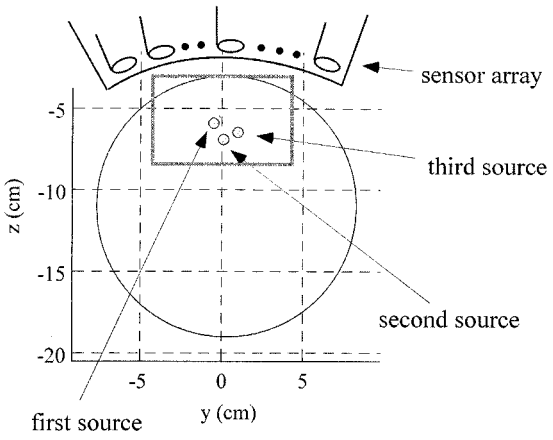

Fig. 1. The coordinate system and the source-detector configuration used in the numerical experiments. The coordinate origin was set at the center of the detector coil located at the center of the coil array. The cross section at $x = 1.0$ is shown. The circle shows the cross section of the sphere used for the forward calculation. The square shows the reconstruction region for the experiments whose results are shown in Figs. 3–6.

TABLE I
SOURCE PARAMETER VALUES USED FOR THE NUMERICAL EXPERIMENTS IN SECTION III

source number	location (cm)	orientation
1	(1.0, −0.5, −5.9)	(1.0, 0., 0.)
2	(1.0, 0.1, −6.9)	(0.7, 0.7, 0.)
3	(1.0, 0.8, −6.7)	(1.0, 0., 0.)

1) Vector-Type Borgiotti–Kaplan Beamformer: The vector-extended Borgiotti–Kaplan beamformer is obtained by using the following constrained minimizations:

$$\min_{\boldsymbol{w}_x} \boldsymbol{w}_x^T \boldsymbol{R}_b \boldsymbol{w}_x$$

subject to

$$\boldsymbol{w}_x^T \boldsymbol{w}_x = 1, \quad \boldsymbol{w}_x^T \boldsymbol{l}_y(\boldsymbol{r}) = 0, \quad \text{and} \quad \boldsymbol{w}_x^T \boldsymbol{l}_z(\boldsymbol{r}) = 0,$$

$$\min_{\boldsymbol{w}_y} \boldsymbol{w}_y^T \boldsymbol{R}_b \boldsymbol{w}_y$$

subject to

$$\boldsymbol{w}_y^T \boldsymbol{l}_x(\boldsymbol{r}) = 0, \quad \boldsymbol{w}_y^T \boldsymbol{w}_y = 1, \quad \text{and} \quad \boldsymbol{w}_y^T \boldsymbol{l}_z(\boldsymbol{r}) = 0,$$

$$\min_{\boldsymbol{w}_z} \boldsymbol{w}_z^T \boldsymbol{R}_b \boldsymbol{w}_z$$

subject to

$$\boldsymbol{w}_z^T \boldsymbol{l}_x(\boldsymbol{r}) = 0, \quad \boldsymbol{w}_z^T \boldsymbol{l}_y(\boldsymbol{r}) = 0, \quad \text{and} \quad \boldsymbol{w}_z^T \boldsymbol{w}_z = 1. \quad (7)$$

We first derive the expression for $\boldsymbol{w}_x$. Let us introduce a scalar constant ξ such that $\boldsymbol{w}_x^T \boldsymbol{l}_x(\boldsymbol{r}) = \xi$ where ξ can be determined from the relationship $\boldsymbol{w}_x^T \boldsymbol{w}_x = 1$. Then, the constrained optimization problem in (7) is changed to

$$\min_{\boldsymbol{w}_x} \boldsymbol{w}_x^T \boldsymbol{R}_b \boldsymbol{w}_x \quad \text{subject to} \quad \boldsymbol{L}^T(\boldsymbol{r}) \boldsymbol{w}_x = \xi \begin{bmatrix} 1 \\ 0 \\ 0 \end{bmatrix} = \xi \boldsymbol{f}_x. \quad (8)$$

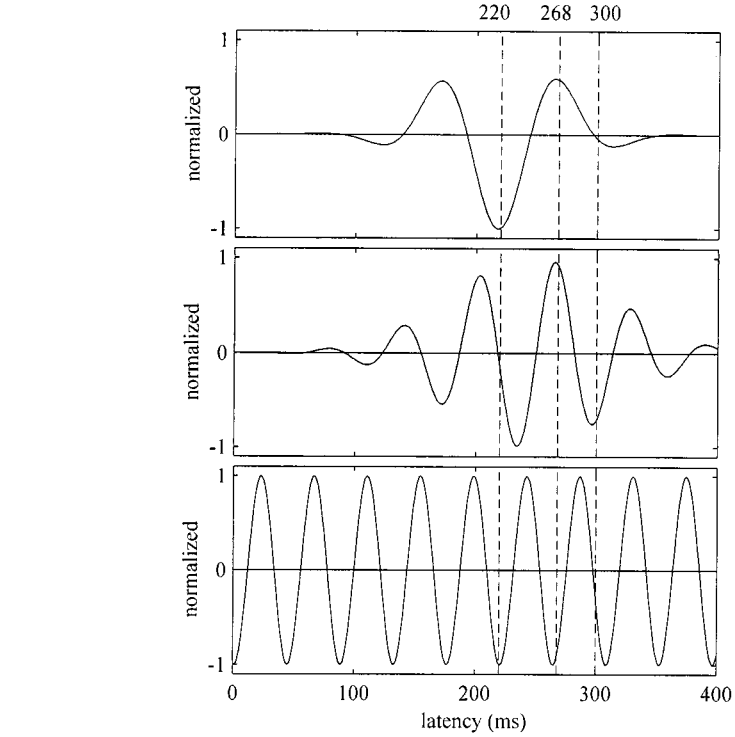

(a)

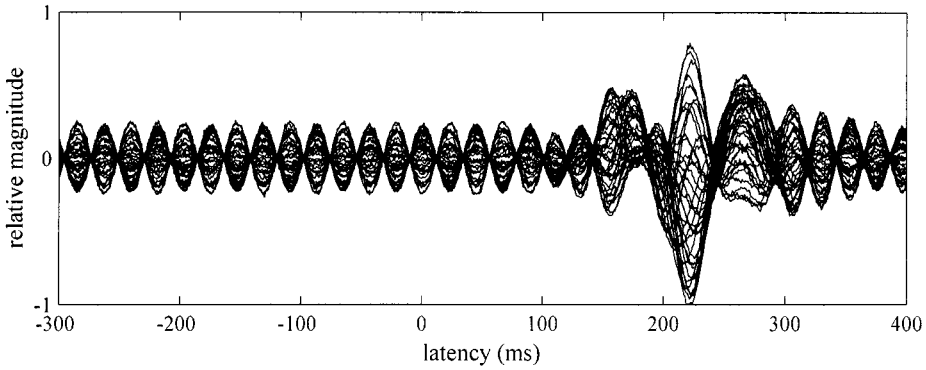

(b)

Fig. 2. (a) Time courses of the three sources assumed in the numerical experiments. Time courses from the first to the third sources are shown from the top to the bottom, respectively. The time courses are shown for the time window between 0 and 400 ms. Each time course is normalized by its maximum value. Three vertical broken lines indicate the time instants 220, 268, and 300 ms at which the source-moment magnitude is displayed in Figs. 3(a)–6(a). (b) The generated magnetic field used for the numerical experiments.

The solution of this optimization problem is known to have the form

$$\boldsymbol{w}_x = \xi \boldsymbol{R}_b^{-1} \boldsymbol{L}(\boldsymbol{r}) \left[\boldsymbol{L}^T(\boldsymbol{r}) \boldsymbol{R}_b^{-1} \boldsymbol{L}(\boldsymbol{r}) \right]^{-1} \boldsymbol{f}_x. \tag{9}$$

Then, we have

$$\boldsymbol{w}_x^T \boldsymbol{w}_x = \xi^2 \boldsymbol{f}_x^T \boldsymbol{\Omega} \boldsymbol{f}_x \tag{10}$$

where

$$\boldsymbol{\Omega} = \left[\boldsymbol{L}^T(\boldsymbol{r}) \boldsymbol{R}_b^{-1} \boldsymbol{L}(\boldsymbol{r}) \right]^{-1} \boldsymbol{L}^T(\boldsymbol{r}) \boldsymbol{R}_b^{-2} \boldsymbol{L}(\boldsymbol{r}) \cdot \left[\boldsymbol{L}^T(\boldsymbol{r}) \boldsymbol{R}_b^{-1} \boldsymbol{L}(\boldsymbol{r}) \right]^{-1}.$$

Thus, we get $\xi = 1/\sqrt{\boldsymbol{f}_x^T \boldsymbol{\Omega} \boldsymbol{f}_x}$ from the relationship $\boldsymbol{w}_x^T \boldsymbol{w}_x = 1$. Using exactly the same derivation, the weights $\boldsymbol{w}_y$ and $\boldsymbol{w}_z$ can be derived, and a set of the weights is expressed as

$$\boldsymbol{w}_\mu = \frac{\boldsymbol{R}_b^{-1} \boldsymbol{L}(\boldsymbol{r}) \left[\boldsymbol{L}^T(\boldsymbol{r}) \boldsymbol{R}_b^{-1} \boldsymbol{L}(\boldsymbol{r}) \right]^{-1} \boldsymbol{f}_\mu}{\sqrt{\boldsymbol{f}_\mu^T \boldsymbol{\Omega} \boldsymbol{f}_\mu}}. \tag{11}$$

It can be shown that the above beamformer retains the property of the Borgiotti–Kaplan beamformer, and its output power is equal to the power of the source activity normalized by the power of the output noise due to the additive sensor noise.

2) Extension to an Eigenspace-Projection Beamformer: The extension to an eigenspace-projection beamformer is attained by projecting the weight vectors in (11) onto

the signal subspace of the measurement covariance matrix. The eigenspace projection improves the output SNR without sacrificing the spatial resolution. The general analysis regarding how this eigenspace projection improves the output SNR has been reported [18].

Unless the source activities are perfectly correlated with each other, $\boldsymbol{R}_b$ has Q eigenvalues greater than σ^2 and $M-Q$ eigenvalues equal to σ^2 where σ^2 is the variance of the additive noise. Assuming that the eigenvalues are numbered in decreasing order, let us define the matrix $\boldsymbol{E}_S$ as $\boldsymbol{E}_S = [\boldsymbol{e}_1, \ldots, \boldsymbol{e}_Q]$, where $\{\boldsymbol{e}_j\}$ with $j = 1, 2, \ldots, M$ are the eigenvectors of $\boldsymbol{R}_b$. The column span of $\boldsymbol{E}_S$ is the maximum-likelihood estimate of the signal subspace of $\boldsymbol{R}_b$ [19]. The weight vectors of the eigenspace-projected beamformer is obtained by using [20]

$$\overline{\boldsymbol{w}}_\mu = \boldsymbol{E}_S \boldsymbol{E}_S^T \boldsymbol{w}_\mu. \tag{12}$$

The projection onto the signal subspace using the above equation, however, invalidates the null constraints imposed on the orthogonal components. This can be understood by considering, for example, the case of $\overline{\boldsymbol{w}}_x$. The null constraints in this case should be $\overline{\boldsymbol{w}}_x^T \boldsymbol{l}_y(\boldsymbol{r}) = 0$ and $\overline{\boldsymbol{w}}_x^T \boldsymbol{l}_z(\boldsymbol{r}) = 0$. However, let us consider

$$\begin{aligned}\overline{\boldsymbol{w}}_x^T \boldsymbol{l}_y(\boldsymbol{r}) &= \left(\boldsymbol{E}_S \boldsymbol{E}_S^T \boldsymbol{w}_x\right)^T \boldsymbol{l}_y(\boldsymbol{r}) = \boldsymbol{w}_x^T \boldsymbol{E}_S \boldsymbol{E}_S^T \boldsymbol{l}_y(\boldsymbol{r}) \\ \overline{\boldsymbol{w}}_x^T \boldsymbol{l}_z(\boldsymbol{r}) &= \left(\boldsymbol{E}_S \boldsymbol{E}_S^T \boldsymbol{w}_x\right)^T \boldsymbol{l}_z(\boldsymbol{r}) = \boldsymbol{w}_x^T \boldsymbol{E}_S \boldsymbol{E}_S^T \boldsymbol{l}_z(\boldsymbol{r}).\end{aligned} \tag{13}$$

Because $\boldsymbol{l}_y(\boldsymbol{r})$ and $\boldsymbol{l}_z(\boldsymbol{r})$ are not necessarily in the signal subspace, we generally have $\boldsymbol{E}_S \boldsymbol{E}_S^T \boldsymbol{l}_y(\boldsymbol{r}) \neq \boldsymbol{l}_y(\boldsymbol{r})$ and $\boldsymbol{E}_S \boldsymbol{E}_S^T \boldsymbol{l}_z(\boldsymbol{r}) \neq \boldsymbol{l}_z(\boldsymbol{r})$ and, therefore, $\boldsymbol{w}_x^T \boldsymbol{E}_S \boldsymbol{E}_S^T \boldsymbol{l}_y(\boldsymbol{r}) \neq 0$ and $\boldsymbol{w}_x^T \boldsymbol{E}_S \boldsymbol{E}_S^T \boldsymbol{l}_z(\boldsymbol{r}) \neq 0$, leading to the relationships $\overline{\boldsymbol{w}}_x^T \boldsymbol{l}_y(\boldsymbol{r}) \neq 0$ and $\overline{\boldsymbol{w}}_x^T \boldsymbol{l}_z(\boldsymbol{r}) \neq 0$. Consequently, we conclude that the signal subspace projector $\boldsymbol{E}_S \boldsymbol{E}_S^T$ does not preserve the null constraints.

It can, however, be shown that the eigenspace-projection beamformer in (12) can detect the three orthogonal components of the source moment even though the null constraints are not preserved. Omitting the time notation, let us decompose the measured magnetic field $\boldsymbol{b}$ into two parts, $\boldsymbol{b} = \boldsymbol{b}^{\mathrm{tar}} + \boldsymbol{b}^{\mathrm{oth}}$ where $\boldsymbol{b}^{\mathrm{tar}}$ is the magnetic field generated from the target source at $\boldsymbol{r}$, and $\boldsymbol{b}^{\mathrm{oth}}$ is the contribution from other sources. The magnetic field $\boldsymbol{b}^{\mathrm{tar}}$ can be expressed as $\boldsymbol{b}^{\mathrm{tar}} = (\eta_x \boldsymbol{l}_x(\boldsymbol{r}) + \eta_x \boldsymbol{l}_y(\boldsymbol{r}) + \eta_z \boldsymbol{l}_z(\boldsymbol{r}))s(t)$, where $[\eta_x, \eta_y, \eta_z]$ expresses the orientation of the target source, and $s(t)$ is its moment magnitude. Then, the estimated x component of the source moment, $\hat{s}_x(t)$, is expressed as $\hat{s}_x(t) = \overline{\boldsymbol{w}}_x^T(\boldsymbol{r})\boldsymbol{b}(t) = \overline{\boldsymbol{w}}_x^T(\boldsymbol{r})\boldsymbol{b}^{\mathrm{tar}} + \overline{\boldsymbol{w}}_x^T(\boldsymbol{r})\boldsymbol{b}^{\mathrm{oth}}$. Since the weight $\overline{\boldsymbol{w}}_x^T(\boldsymbol{r})$ does not pass the signal other than that from $\boldsymbol{r}$, we have $\overline{\boldsymbol{w}}_x^T(\boldsymbol{r})\boldsymbol{b}^{\mathrm{oth}} = 0$ and, consequently

$$\begin{aligned}\hat{s}_x(t) &= \overline{\boldsymbol{w}}_x^T(\boldsymbol{r})\boldsymbol{b}^{\mathrm{tar}} \\ &= \boldsymbol{w}_x^T \boldsymbol{E}_S \boldsymbol{E}_S^T (\eta_x \boldsymbol{l}_x(\boldsymbol{r}) + \eta_x \boldsymbol{l}_y(\boldsymbol{r}) + \eta_z \boldsymbol{l}_z(\boldsymbol{r}))s(t).\end{aligned} \tag{14}$$

Because the vector $(\eta_x \boldsymbol{l}_x(\boldsymbol{r}) + \eta_x \boldsymbol{l}_y(\boldsymbol{r}) + \eta_z \boldsymbol{l}_z(\boldsymbol{r}))$ is in the signal subspace, we get

$$\begin{aligned}&\boldsymbol{E}_S \boldsymbol{E}_S^T (\eta_x \boldsymbol{l}_x(\boldsymbol{r}) + \eta_x \boldsymbol{l}_y(\boldsymbol{r}) + \eta_z \boldsymbol{l}_z(\boldsymbol{r})) \\ &\quad = (\eta_x \boldsymbol{l}_x(\boldsymbol{r}) + \eta_x \boldsymbol{l}_y(\boldsymbol{r}) + \eta_z \boldsymbol{l}_z(\boldsymbol{r})).\end{aligned} \tag{15}$$

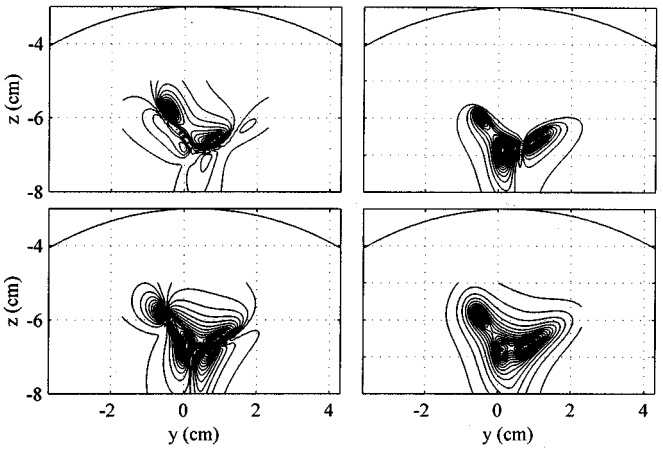

(a)

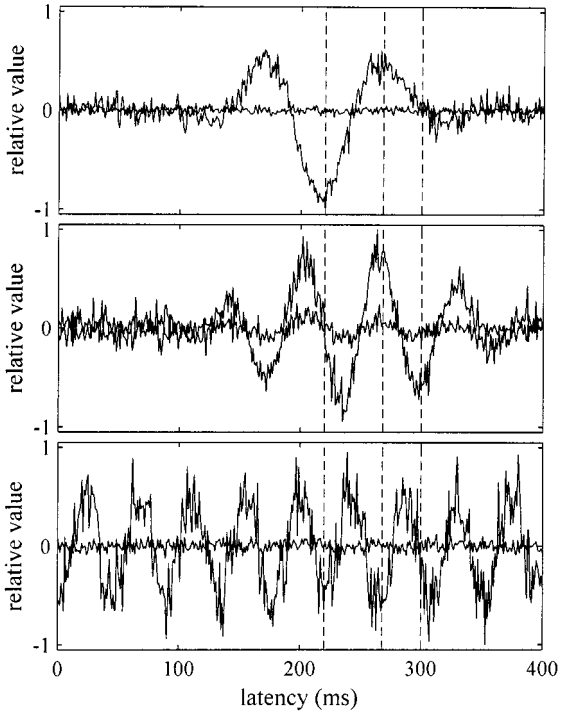

(b)

Fig. 3. (a) Results of the spatio-temporal reconstruction obtained using the minimum-variance-based vector beamformer in (6). The upper-left, upper-right, and lower-left maps respectively show the snapshots of the source-moment magnitude at 220, 268, and 300 ms. The lower-right map shows the time-averaged reconstruction. (b) Estimated time courses from the first to the third sources are shown from the top to the bottom, respectively. The three vertical broken lines indicate the time instants of 220, 268, and 300 ms.

Therefore, we finally get

$$\begin{aligned}\hat{s}_x(t) &= \overline{\boldsymbol{w}}_x^T(\boldsymbol{r})\boldsymbol{b}^{\mathrm{tar}} \\ &= \boldsymbol{w}_x^T(\eta_x \boldsymbol{l}_x(\boldsymbol{r}) + \eta_x \boldsymbol{l}_y(\boldsymbol{r}) + \eta_z \boldsymbol{l}_z(\boldsymbol{r}))s(t) \\ &= \eta_x s(t)\left(\boldsymbol{w}_x^T \boldsymbol{l}_x(\boldsymbol{r})\right) \propto \eta_x s(t).\end{aligned} \tag{16}$$

Similarly, we can also obtain $\hat{s}_y(t) = \overline{\boldsymbol{w}}_y^T \boldsymbol{b}(t) \propto \eta_y s(t)$ and $\hat{s}_z(t) = \overline{\boldsymbol{w}}_z^T \boldsymbol{b}(t) \propto \eta_z s(t)$. Thus, the eigenspace-projection beamformer in (12) can detect the three orthogonal components of the source moment, even though the null constraints are not preserved.

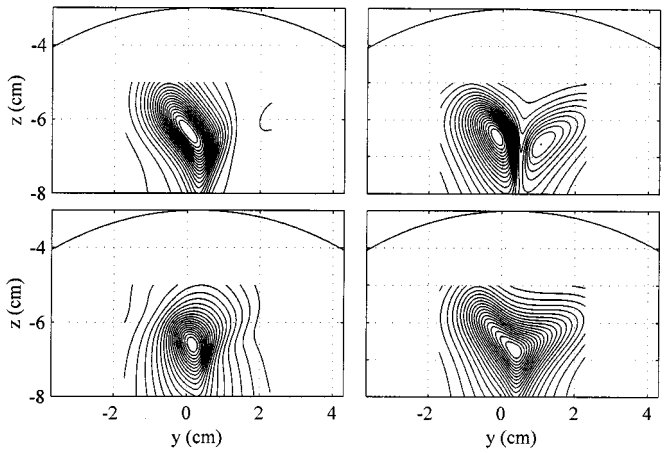

(a)

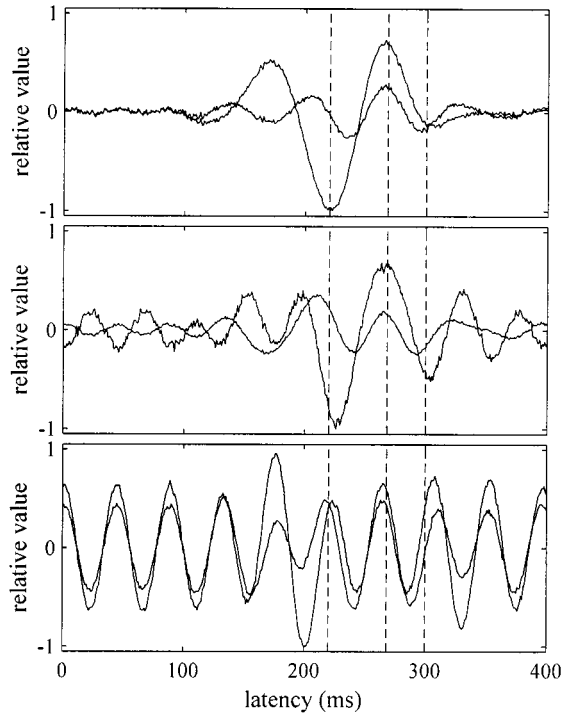

(b)

Fig. 4. (a) Results of the spatio-temporal reconstruction obtained using the minimum-variance-based vector beamformer in (6) together with the use of the regularized inverse $(\boldsymbol{R}_b + \gamma \boldsymbol{I})^{-1}$. The parameter γ was set at $0.003\lambda_1$, where λ_1 is the largest eigenvalue of $\boldsymbol{R}_b$. The upper-left, upper-right, and lower-left maps respectively show the snapshots of the source-moment magnitude at 220, 268, and 300 ms. The lower-right map shows the time-averaged reconstruction. (b) Estimated time courses from the first to the third sources are shown from the top to the bottom, respectively. The three vertical broken lines indicate the time instants of 220, 268, and 300 ms.

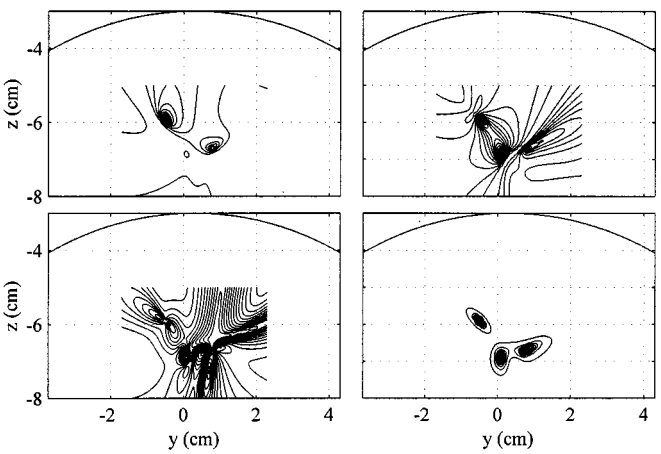

(a)

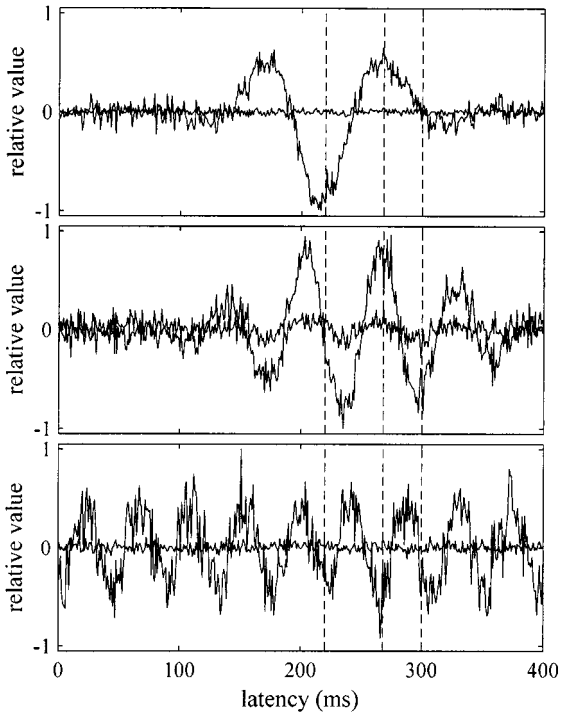

(b)

Fig. 5. (a) Results of the spatio-temporal reconstruction with the weight vectors obtained using (11) alone. The upper-left, upper-right, and lower-left maps respectively show the snapshots of the source-moment magnitude at 220 ms, 268 ms, and 300 ms. The lower-right map shows the time-averaged reconstruction. (b) Estimated time courses from the first to the third sources are shown from the top to the bottom, respectively. The three vertical broken lines indicate the time instants of 220, 268, and 300 ms.

III. Numerical Experiments

A. Data Generation

We conducted a series of numerical experiments to test the effectiveness of the proposed method. A coil alignment of the 37-channel Magnes biomagnetic measurement system (Biomagnetic Technologies Inc., San Diego, CA) was used in these experiments. The coordinate system used in our numerical experiments is illustrated in Fig. 1. The values of the spatial coordinates (x, y, z) were expressed in centimeters. Three signal sources were assumed to exist on a plane defined as $x =$ 1.0. The locations as well as the orientations of the sources are listed in Table I. Because a spherical homogeneous conductor [3] with the origin set at $(1, 0, -11)$ was used, we express the source-moment vector using the two tangential components (θ, ϕ).

The magnetic field was generated at a 1-ms interval from -300 to 400 ms. The moment time courses of the three sources are shown in Fig. 2(a) for the time window between 0 and 400 ms. The white Gaussian noise was added to the generated magnetic field, and the SNR, defined as the ratio of the Frobenius norm of the signal-magnetic-field data matrix to that of

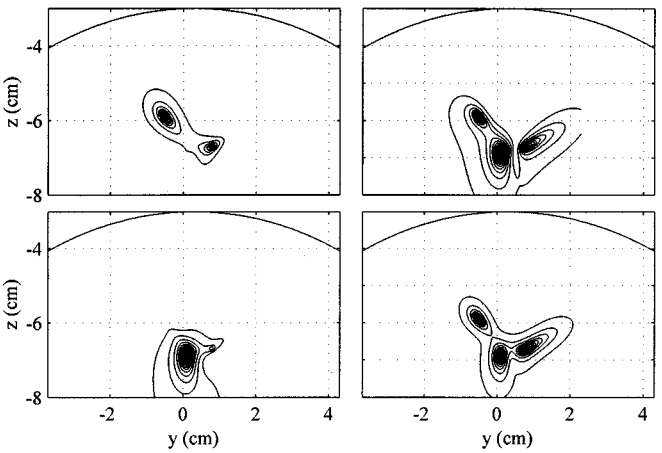

(a)

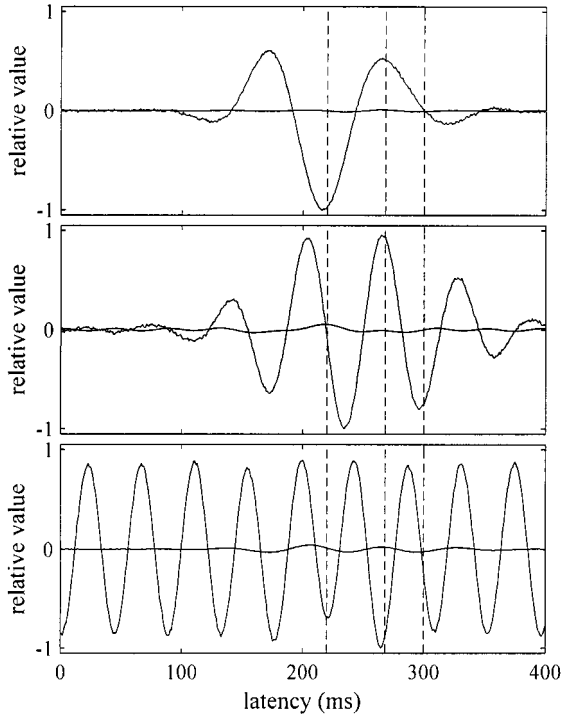

(b)

Fig. 6. (a) Results of the spatio-temporal reconstruction obtained using the proposed vector beamformer technique [(11) and (12)]. The upper-left, upper-right, and lower-left maps respectively show the snapshots of the source-moment magnitude at 220, 268, and 300 ms. The lower-right map shows the time-averaged reconstruction. (b) Estimated time courses from the first to the third sources are shown from the top to the bottom, respectively. The three vertical broken lines indicate the time instants of 220, 268, and 300 ms.

the noise matrix, was set to 18. The generated magnetic field is shown in Fig. 2(b). This SNR is higher than that in typical cases of actual MEG measurements. We used such a high SNR value because the differences in the source estimation results obtained using tested beamformer techniques can be more easily observed under such high SNR conditions; such differences might otherwise be obscured by noise effects.

B. Spatio-Temporal Reconstruction Experiments

The spatio-temporal reconstruction was performed by using

$$\hat{s}_\phi(\boldsymbol{r}, t) = \boldsymbol{w}_\phi^T(\boldsymbol{r})\boldsymbol{b}(t) \quad \text{and} \quad \hat{s}_\theta(\boldsymbol{r}, t) = \boldsymbol{w}_\theta^T(\boldsymbol{r})\boldsymbol{b}(t). \quad (17)$$

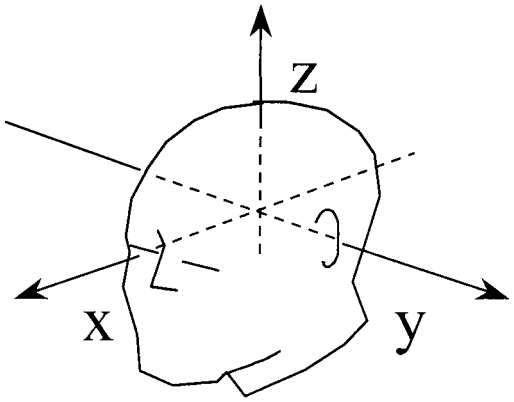

Fig. 7. The x, y, and z coordinates used to express the reconstruction results in Section IV. The midpoint between the left and right preauricular points was defined as the coordinate origin. The axis directed away from the origin toward the left preauricular point was defined as the $+y$ axis, and that from the origin to the nasion was the $+x$ axis. The $+z$ axis was defined as the axis perpendicular to both these axes and was directed from the origin to the vertex.

Note that since these weight vectors are calculated for any spatial location $\boldsymbol{r}$, the source-moment distribution at any location can be reconstructed in a perfectly post-processing manner. The reconstruction region was set as an area defined by $-4 \le y \le 4$ and $-8 \le z \le -3$ on the plane $x = 1$ (as indicated by the square in Fig. 1), and the reconstruction interval was 1 mm in the y and z directions.

Once $\hat{s}_\phi(\boldsymbol{r}, t)$ and $\hat{s}_\theta(\boldsymbol{r}, t)$ were obtained, an angle representing the mean source direction in the $\phi - \theta$ plane, ρ, was calculated using

$$\rho = \arctan\left(\sqrt{\frac{\langle \hat{s}_\theta(t)^2 \rangle}{\langle \hat{s}_\phi(t)^2 \rangle}}\right), \quad \text{if} \quad \frac{\langle \hat{s}_\theta(t) \rangle}{\langle \hat{s}_\phi(t) \rangle} \ge 0$$

$$\rho = -\arctan\left(\sqrt{\frac{\langle \hat{s}_\theta(t)^2 \rangle}{\langle \hat{s}_\phi(t)^2 \rangle}}\right), \quad \text{if} \quad \frac{\langle \hat{s}_\theta(t) \rangle}{\langle \hat{s}_\phi(t) \rangle} < 0 \quad (18)$$

where $\langle \cdot \rangle$ indicates the average over the time window with which $\boldsymbol{R}_b$ was calculated. Then, the time course expressed in the mean source direction, $\hat{s}_{\|}(\boldsymbol{r}, t)$, and that in its orthogonal direction, $\hat{s}_\perp(\boldsymbol{r}, t)$ were given by

$$\hat{s}_{\|}(\boldsymbol{r}, t) = \hat{s}_\phi(\boldsymbol{r}, t)\cos(\rho) + \hat{s}_\theta(\boldsymbol{r}, t)\sin(\rho)$$

$$\hat{s}_\perp(\boldsymbol{r}, t) = \hat{s}_\theta(\boldsymbol{r}, t)\cos(\rho) - \hat{s}_\phi(\boldsymbol{r}, t)\sin(\rho). \quad (19)$$

In the following experiments, we used $\hat{s}_{\|}(\boldsymbol{r}, t)$ and $\hat{s}_\perp(\boldsymbol{r}, t)$ when displaying the time course of a source activity.

To display the results of the spatio-temporal reconstruction, three time points at 220, 268, and 300 ms [marked in Fig. 2(a)] were selected. The amplitude of the second source happened to be zero at 220 ms, all the sources had nonzero amplitudes at 268 ms, and only the second source had a nonzero amplitude at 300 ms. The snapshots of the source magnitude distribution $|\hat{s}(\boldsymbol{r}, t)| = \sqrt{\hat{s}_\phi^2(\boldsymbol{r}, t) + \hat{s}_\theta^2(\boldsymbol{r}, t)}$ at these three time points, and the time averaged reconstruction $\sqrt{\langle \hat{s}(\boldsymbol{r}, t)^2 \rangle}$ were displayed in the following experiments.

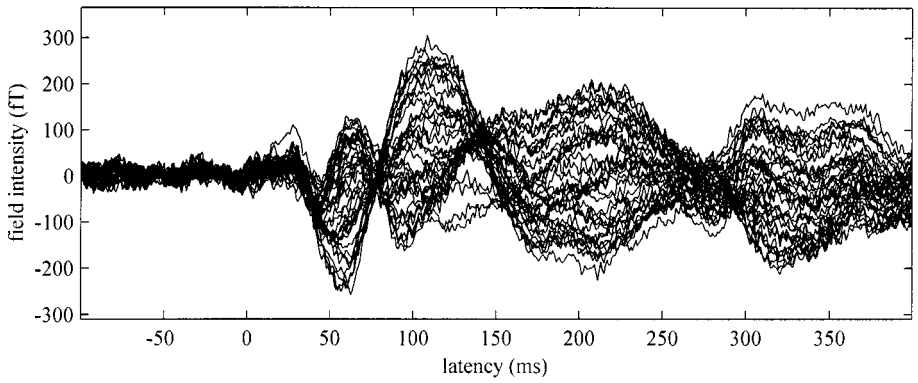

Fig. 8. The auditory-somatosensory combined response measured by simultaneously applying an auditory stimulus and a somatosensory stimulus. The auditory stimulus was a 1-kHz pure tone delivered to the subject's right ear and the somatosensory stimulus was a 30-ms-duration tactile pulse delivered to the distal segment of the right index finger. A total of 256 epochs were averaged.

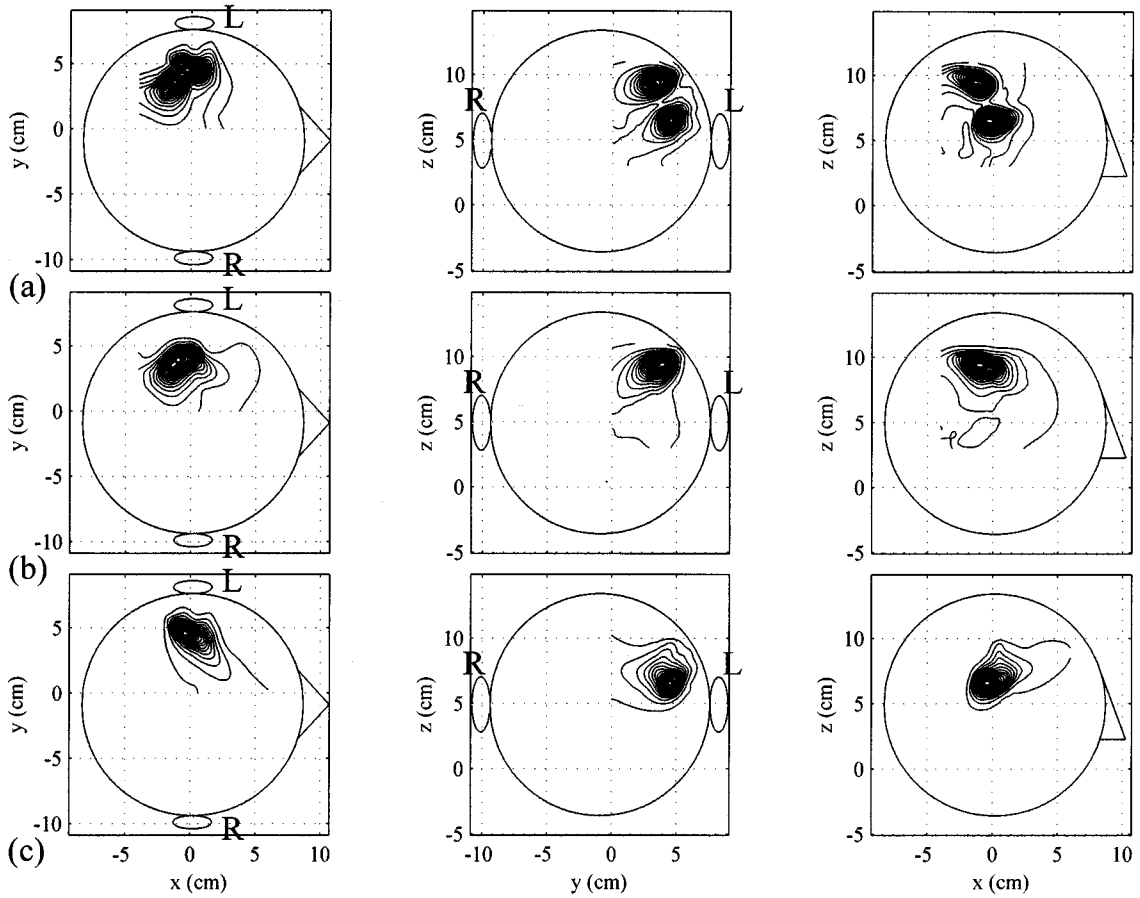

Fig. 9. Results of the spatio-temporal reconstruction from the auditory-somatosensory combined response in Fig. 8. The reconstruction was obtained using the proposed beamformer. The maximum intensity projection of the source-moment magnitude onto the axial (left), coronal (middle), and sagittal (right) slices are displayed. The source-magnitude distributions are shown at latencies of (a) 65 ms, (b) 138 ms, and (c) 194 ms. These time instants are shown by the vertical broken lines in Fig. 10.

C. Results from Minimum-Variance Vector Beamformer

The results of the spatio-temporal reconstruction obtained using the minimum-variance vector beamformer in (6) with the normalized lead field matrix are shown in Fig. 3(a). The estimated time courses at the pixels nearest to the three source locations are shown in Fig. 3(b). These results show that the reconstruction at each instant in time was fairly noisy: the snapshot at 220 ms showed some influence from the second source, and the snapshot at 300 ms contained the activities of the first and third sources. The time-averaged reconstruction, however, clearly resolved three active sources. Note that this time-averaged reconstruction is equal to the map of the neural activity index proposed in [10],

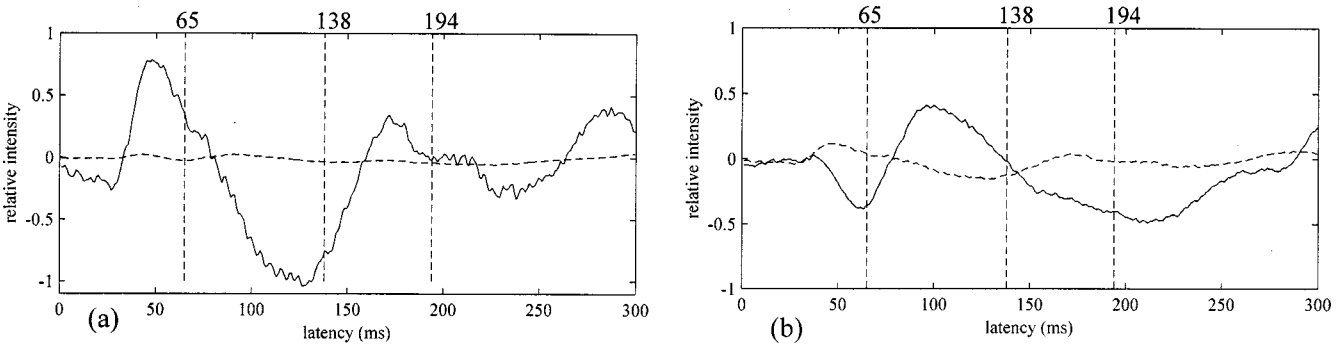

Fig. 10. Time courses of the points nearest to (a) the primary somatosensory cortex and (b) the primary auditory cortex. The solid and broken plotted lines correspond, respectively, to $\hat{s}_{||}(\boldsymbol{r}, t)$ and $\hat{s}_{\perp}(\boldsymbol{r}, t)$. Three vertical broken lines indicate the time instants of 65, 138, and 194 ms.

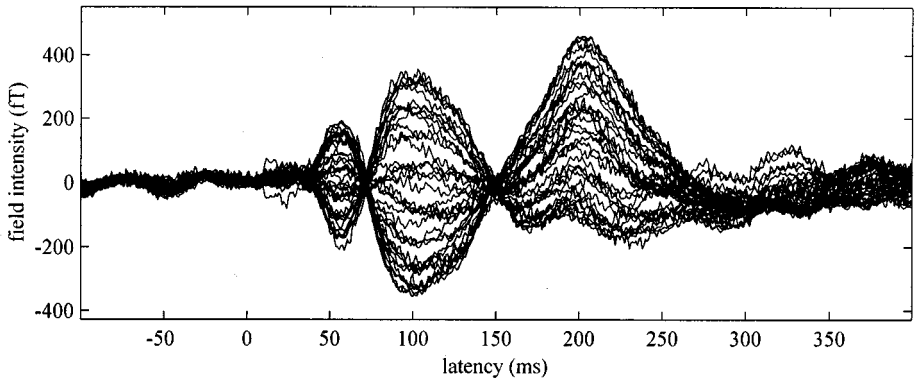

Fig. 11. The auditory-button-press response. The data was measured with a subject who pressed a response button with his left index finger when he heard the 1-kHz pure tone delivered to his right ear. A total of 256 epochs are averaged.

because the noise was white Gaussian and the noise covariance matrix was expressed as the unit matrix in these numerical experiments.

It is known that this poor output SNR is due to the use of the direct matrix inversion $\boldsymbol{R}_b^{-1}$ [11], [12], [16]. Thus, we next tested the minimum-variance beamformer together with the use of the regularized inverse $(\boldsymbol{R}_b + \gamma \boldsymbol{I})^{-1}$ instead of $\boldsymbol{R}_b^{-1}$. The regularization parameter was set at $0.003\lambda_1$, where λ_1 is the largest eigenvalue of $\boldsymbol{R}_b$. The results in Fig. 4(a) show that a considerable amount of blur was introduced. The estimated time courses are shown in Fig. 4(b). Fig. 4 shows that the SNR of the beamformer output was considerably increased in this case, although each time course shows some influence from neighboring sources. The results here demonstrated that the regularization leads to a tradeoff between the spatial resolution and the SNR of the beamformer output.

D. Results from Proposed Vector Beamformer

We first show the reconstruction results from weight vectors obtained using (11) alone. This is equivalent to the vector-extended Borgiotti–Kaplan beamformer without the eigenspace projection. The results are shown in Fig. 5. Comparison between the time-averaged reconstruction in Fig. 3(a) and that in Fig. 5(a) confirms that the Borgiotti–Kaplan-type beamformer has a spatial resolution much higher than the minimum-variance beamformer. The spatio-temporal reconstruction, however, is very noisy for both cases.

We then applied the proposed vector beamformer obtained using (11) and (12) to the same computer-generated data set. The reconstructed source distributions are shown in Fig. 6(a), and the estimated time courses are shown in Fig. 6(b). Comparison between Figs. 5 and 6 confirms that the eigenspace projection can improve the SNR with almost no sacrifice of the spatial resolution. Comparing the results in Fig. 6 with the minimum-variance results in Fig. 3, we can clearly see that the proposed beamformer technique significantly improved both spatial resolution and output SNR.

IV. Application to Auditory-Evoked MEG Data

We applied the proposed beamformer technique to two sets of auditory-evoked MEG data to demonstrate its spatio-temporal reconstruction capability. The auditory-evoked fields were measured using the 37-channel Magnes biomagnetometer installed at the Biomagnetic Imaging Laboratory, University of California, San Francisco. The auditory stimulus was presented to the subject's right ear. The sensor array was placed above the subject's left hemisphere with the position adjusted to optimally record the N1m auditory-evoked field. The average inter-stimulus interval was 2 s, with the interval randomly varied between 1.75 s and 2.25 s. The sampling frequency was set at 1 kHz. An on-line filter with a bandwidth from 1 to 400 Hz was used, and no post-processing digital filter was applied. To express the results of reconstructing source activities in this section, we used the head coordinate system illustrated in Fig. 7.

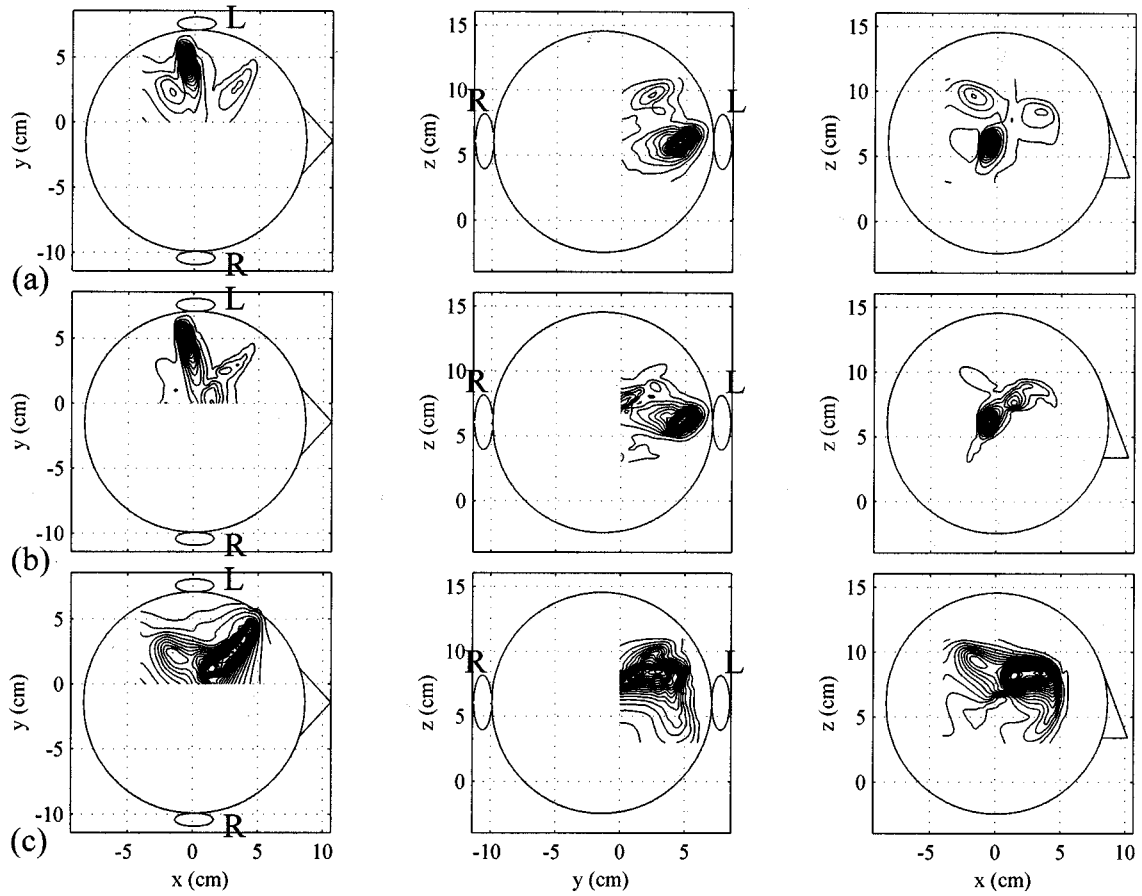

Fig. 12. Results of the spatio-temporal reconstruction from the auditory-button-press response in Fig. 11. The maximum intensity projection of the source-moment magnitude onto the axial (left), coronal (middle), and sagittal (right) slices are displayed. The source-magnitude distributions are shown at latencies of (a) 100 ms, (b) 170 ms, and (c) 200 ms. These time instants are shown by the vertical broken lines in Fig. 13.

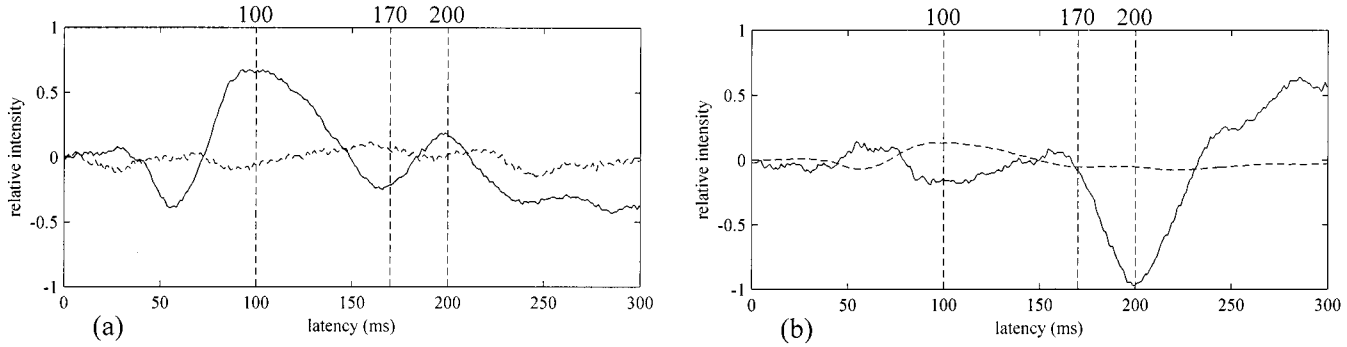

Fig. 13. Time courses of the points nearest to (a) the primary auditory cortex and (b) the center of the motor activities. The solid and broken plotted lines correspond, respectively, to $\hat{s}_{\parallel}(\boldsymbol{r}, t)$ and $\hat{s}_{\perp}(\boldsymbol{r}, t)$. Three vertical broken lines indicate the time instants of 100, 170, and 200 ms.

The first data we tested was the auditory-somatosensory combined response measured by simultaneously applying an auditory stimulus and a somatosensory stimulus to a male subject. The auditory stimulus was a 1-kHz pure tone with a 200-ms duration, and the somatosensory stimulus was a 30-ms-duration tactile pulse (17 psi) delivered to the distal segment of the right index finger. These two stimuli started at the same time. A total of 256 epochs were measured, and the response averaged over all the epochs is shown in Fig. 8. We applied the proposed beamformer to this averaged data. The data in the time window ranging from 0 to 300 ms was used for calculating the covariance matrix $\boldsymbol{R}_b$. The signal subspace dimension Q was set at two because the eigenvalue spectrum of $\boldsymbol{R}_b$ showed two distinctly large eigenvalues.

The reconstructed source-magnitude maps at three latencies, 65, 138, and 194 ms, are shown in Fig. 9. The source magnitude map at 138 ms [Fig. 9(b)] contains a source activity presumably at the primary somatosensory cortex. The source magnitude map at 194 ms [Fig. 9(c)] shows a source activity at the

primary auditory cortex. The map at 65 ms [Fig. 9(a)] contains both of these activities.

The time courses of the points at the primary somatosensory and auditory cortices are shown in Fig. 10(a) and (b), respectively. The coordinates of these cortices were determined from the maximum points in Fig. 9(b) and (c). Both $\hat{s}_{||}(t)$ and $\hat{s}_{\perp}(t)$ were plotted in Fig. 10 so that we could check whether the orientation of the source was fixed or changed during the time window with which $\boldsymbol{R}_b$ was calculated. In Fig. 10(a) the P50 peak, which is known to represent activity of the primary somatosensory cortex, is observed near the latency of 50 ms. In Fig. 10(b), the auditory N1m peak is observed near the latency of 100 ms. These time course plots also show that both sources were active at 65 ms, that only the primary somatosensory area was active at 138 ms, and that only the primary auditory area was active at 194 ms. These observations are consistent with the source-activity behavior shown in Fig. 9(a)–(c).

We next applied the proposed beamformer to auditory-button-press data. When we measured this data set, the subject pressed a response button with his left index finger when he heard the 1-kHz pure tone. Thus, the data should contain motor activities fairly closely time-locked to the auditory stimulus. The results obtained by averaging a total of 256 epochs are shown in Fig. 11. The proposed beamformer was applied to this averaged auditory-button-press data. The data from a time window ranging from 0 to 300 ms was used for calculating $\boldsymbol{R}_b$ and the signal subspace dimension was set at two. The results of the reconstruction are shown in Fig. 12. Here, the reconstructed source-magnitude distribution at 100 ms is shown in Fig. 12(a), that at 170 ms is shown in Fig. 12(b), and that at 200 ms is shown in Fig. 12(c). The reconstructed results at 100 ms contained clear activity near the primary auditory cortex in the left temporal area. The results at 170 ms showed that the activity at the primary auditory area was still dominant. The results at 200 ms showed wide-spread activities, presumably around motor and premotor areas.

We determined the location of the primary auditory area by choosing the maximum point in Fig. 12(a), and the location of the center of the motor activities by choosing the maximum point in Fig. 12(c). The time course of the activity in the primary auditory area is shown in Fig. 13(a). The time course forms a peak near the latency around 100 ms, clearly showing the auditory N1m component. The auditory activity was relatively weak, but still dominant at the latency of 170 ms. The time course of the motor activities is shown in Fig. 13(b), which indicates that the motor activity formed a peak near 200 ms. These plots are also consistent with the results in Fig. 12.

V. Conclusion

We have developed a novel MEG vector beamformer technique suitable for reconstructing spatio-temporal activities of neural sources. The developed beamformer is formulated in a two-step procedure: the first step extends the Borgiotti–Kaplan beamformer to the vector-type beamformer and the second step projects its weight vectors onto the signal subspace of the measurement covariance matrix. The proposed beamformer has the spatial resolution and the output SNR, both significantly higher than those of the minimum-variance vector beamformer used in the previous investigations. Our numerical experiments verified the superiority of the proposed method, and its application to two sets of auditory MEG data demonstrated the method's spatio-temporal reconstruction capability.

Acknowledgment

The authors would like to thank Dr. T. Roberts and S. Honma for their help in performing the auditory MEG measurements.

References

[1] M. Hämäläinen, R. Hari, R. J. IImoniemi, J. Knuutila, and O. V. Lounasmaa, "Magnetoencephalography-theory, instrumentation, and applications to noninvasive studies of the working human brain," *Rev. Mod. Phys.*, vol. 65, pp. 413–497, 1993.

[2] T. P. L. Roberts, D. Poeppel, and H. A. Rowley, "Magnetoencephalography and magnetic source imaging," *Neuropsychiatry, Neuropsych.., Behavioral Neurol.*, vol. 11, pp. 49–64, 1998.

[3] J. Sarvas, "Basic mathematical and electromagnetic concepts of the biomagnetic inverse problem," *Phys. Med. Biol.*, vol. 32, pp. 11–22, 1987.

[4] M. S. Hämäläinen and R. J. Ilmoniemi, "Interpreting measured magnetic fields of the brain: Estimates of current distributions," Helsinki Univ. Technol., Helsinki, Finland, Tech. Rep. TKK-F-A559, 1984.

[5] R. D. Pascual-Marqui and C. M. Michel, "Low resolution electromagnetic tomography: A new method for localizing electrical activity in the brain," *Int. J. Psychophysiol.*, vol. 18, pp. 49–65, 1994.

[6] K. Uutela, M. Hämäläinen, and E. Somersalo, "Visualization of magnetoencephalographic data using minimum current estimate," *NeuroImage*, vol. 10, pp. 173–180, 1999.

[7] I. F. Gorodnitsky and B. D. Rao, "Sparse signal reconstruction from limited data using FOCUSS: A re-weighted minimum norm algorithm," *IEEE Trans. Signal Processing*, vol. 45, pp. 600–616, Mar. 1997.

[8] B. D. Van Veen and K. M. Buckley, "Beamforming: A versatile approach to spatial filtering," *IEEE Acoust. Speech, Signal Processing Mag.*, vol. 5, pp. 4–24, Apr. 1988.

[9] M. E. Spencer, R. M. Leahy, J. C. Mosher, and P. S. Lewis, "Adaptive filters for monitoring localized brain activity from surface potential time series," in *Proc. 26th Annu. Asilomer Conf. Signals, Systems, and Computers*, Nov. 1992, pp. 156–161.

[10] B. D. Van Veen, W. van Drongelen, M. Yuchtman, and A. Suzuki, "Localization of brain electrical activity via linearly constrained minimum variance spatial filtering," *IEEE Trans. Biomed. Eng.*, vol. 44, pp. 867–880, Sept. 1997.

[11] S. E. Robinson and J. Vrba, "Functional neuroimaging by synthetic aperture magnetometry (SAM)," in *Recent Advances in Biomagnetism*, T. Yoshimoto, *et al.*, Eds. Sendai, Japan: Tohoku Univ. Press, 1999, pp. 302–305.

[12] J. Gross and A. A. Ioannides, "Linear transformations of data space in MEG," *Phys. Med. Biol.*, vol. 44, pp. 2081–2097, 1999.

[13] G. Borgiotti and L. J. Kaplan, "Superresolution of uncorrelated interference sources by using adaptive array technique," *IEEE Trans. Antennas Propagat.*, vol. AP-27, pp. 842–845, 1979.

[14] J. Capon, "High-resolution frequency wavenumber spectrum analysis," *Proc. IEEE*, vol. 57, pp. 1408–1419, 1969.

[15] K. Sekihara, D. Poeppel, and Y. Miyashita, "Application of eigenspace beamformer to virtual depth-electrode measurement using MEG," in *Proc. 2nd Int. Symp. Noninvasive Functional Source Imaging Within the Human Brain and Heart (Biomedizinische Technik)*, S. Supek, Ed., Zagreb, Croatia, Sept. 1999, pp. 127–130.

[16] H. Cox, R. M. Zeskind, and M. M. Owen, "Robust adaptive beamforming," *IEEE Trans. Signal Process.*, vol. SP–35, pp. 1365–1376, 1987.

[17] B. D. Carlson, "Covariance matrix estimation errors and diagonal loading in adaptive arrays," *IEEE Trans. Aerosp. Electron. Syst.*, vol. 24, pp. 397–401, July 1988.

[18] L. Chang and C. C. Yeh, "Performance of DMI and eigenspace-based beamformers," *IEEE Trans. Antennas Propagat.*, vol. 40, pp. 1336–1347, Nov. 1992.

[19] L. L. Scharf, *Statistical Signal Processing: Detection, Estimation, and Time Series Analysis*. New York: Addison-Wesley, 1991.

[20] D. D. Feldman and L. J. Griffiths, "A constrained projection approach for robust adaptive beamforming," in *Proc. Int. Conf. Acoust., Speech, and Signal Processing*, Toronto, Canada, May 1991, pp. 1357–1360.

Kensuke Sekihara (M'88) received the M.S. degree in 1976 and the Ph.D. degree in 1987 both from Tokyo Institute of Technology, Tokyo, Japan.

From 1976 to 2000, he worked with Central Research Laboratory, Hitachi, Ltd., Tokyo, Japan. He was a visiting Research Scientist at Stanford University, Stanford, CA, from 1985 to 1986, and at Basic Development, Siemens Medical Engineering, Erlangen, Germany, from 1991 to 1992. From 1996 to 2000, He worked with "Mind Articulation" research project sponsored by Japan Science and Technology Corporation. He is currently Professor at Tokyo Metropolitan Institute of Technology, Tokyo, Japan. His research interests include the biomagnetic inverse problems, and statistical estimation theory, especially its application to noninvasive functional neuroimaging.

Dr. Sekihara is a member of the IEEE Medicine and Biology Society, and the IEEE Signal Processing Society.

Srikantan S. Nagarajan received the B.S. degree in electrical engineering from the University of Madras, Madras, India, and the M.S. and Ph.D degrees from the Department of Biomedical Engineering at Case Western Reserve University, Cleveland, OH, in 1993 and 1995, respectively.

From 1995-1998, he was a Post-doctoral Fellow in the Keck Center for Integrative Neuroscience at the University of California, San Francisco (UCSF). In 1999, he was a full-time Research Scientist at Scientific Learning Corporation, Berkeley, CA, and an Adjunct Assistant Professor in the Department of Otolaryngology at UCSF. He is currently an Assistant Professor in the Department of Bioengineering at the University of Utah, Salt Lake City. His research interests in neural engineering include bioelectromagnetism, systems and computational neuroscience, and statistical signal processing.

David Poeppel received the B.S. and Ph.D degrees in cognitive neuroscience from Massachusetts Institute of Technology, Cambridge, in 1990 and 1995, respectively.

He is currently an Assistant Professor in the Departments of Linguistics and Biology at the University of Maryland at College Park. His research uses the functional neuroimaging methods magnetoencephalography (MEG), electroencephalography (EEG, positron emission tomography (PET), and functional magnetic resonance imaging (fMRI) to investigate the neural basis of speech and language processing.

Alec Marantz received the B.A. degree in psycholinguistics from Oberlin College, Oberlin, OH, in 1978 and the Ph.D. degree in linguistics from the Massachusetts Institute of Technology (M.I.T.), Cambridge, MA, in 1981.

He joined the faculty at M.I.T. in 1990, where he is currently Professor of Linguistics and Head of the Department of Linguistics and Philosophy. His research interests include the syntax and morphology of natural languages, linguistic universals, and the neurobiology of language. He is currently involved in revising morphological theory within linguistics and in exploring MEG techniques to uncover how the brain process language.

Yasushi Miyashita received the Ph. D. degree in physiology from the University of Tokyo, Tokyo, Japan, in 1979.

He is currently Professor and Chairman of the Physiology Department, the University of Tokyo School of Medicine, Tokyo, Japan. His reserach interests include neural basis of cognition in primates, functional imaging, and image processing with MRI, MEG, and optical devices.